Draft version March 22, 2017
Preprint typeset using LaTeX style emulateapj v. 12/16/11

THE SPIN OF THE SUPERMASSIVE BLACK HOLE IN MCG-05-23-16

Yu Wang[1], M. Ghasemi-Nodehi[1], Matteo Guainazzi[2], and Cosimo Bambi[1,3,†]
[1] Center for Field Theory and Particle Physics and Department of Physics, Fudan University, 200433 Shanghai, China
[2] ESTEC, European Space Agency, 2201AZ Noordwijk, The Netherlands
[3] Theoretical Astrophysics, Eberhard-Karls Universität Tübingen, 72076 Tübingen, Germany

Draft version March 22, 2017

ABSTRACT

We present the results of a multi-epoch and multi-instrument study of the supermassive black hole at the center of the galaxy MCG-05-23-16 aiming at the determination of its spin. We have analyzed high quality X-ray data of MCG-05-23-16 from XMM-Newton, Suzaku, and NuSTAR obtained over a period of about 10 years. We have built a double-reflection spectral model that well describes the observed spectrum based on prior results suggesting that the iron Kα line includes both a broad component from the disk's reflection spectrum and a narrow component due to fluorescence and scattering off material by more distant matter. Our measurement of the black hole spin parameter is $a_* = 0.856 \pm 0.006$ (99% confidence level).

Subject headings: Galaxies: Seyferts – Galaxies: active – X-rays: galaxies – X-ray individual: MCG-05-23-16

1. INTRODUCTION

Black holes should be completely characterized by only two parameters, namely the mass, M, and the spin angular momentum, J, of the compact object (Narayan 2005). The dimensionless spin parameter is defined as $a_* = Jc/(G_{\rm N}M^2)$, where c is the speed of light, $G_{\rm N}$ is Newton's gravitational constant, and $|a_*| \leq 1$ is the condition for the existence of the event horizon. Both M and a_* can evolve with time due to the processes of accretion and merger, but not over our observational timescales.

The mass M sets the size of the system. For stellar-mass black holes, M can be inferred by studying the motion of the stellar companion. In the case of supermassive black holes, we can measure M by studying the motion of stars or gas orbiting the object. The spin parameter a_* determines the properties of the gravitational field around the black hole and can be measured by studying the strong gravity region, where relativistic effects show up. The three main techniques to estimate the spins of black holes are currently the continuum-fitting method (Zhang et al. 1997; McClintock et al. 2011, 2014), the analysis of the reflection spectrum (Brenneman & Reynolds 2006; Brenneman 2013; Reynolds 2014), and the study of quasi-periodic oscillations (QPOs) (Wagoner et al. 2001; Török et al. 2005; Motta et al. 2014).

In the case of supermassive black holes, X-ray reflection spectroscopy is currently the only available technique to infer the value of their spins. The continuum-fitting method requires the analysis of the thermal spectrum of the accretion disk. For supermassive black holes, the spectrum is in the optical/UV band, where extinction and dust absorption limit the ability to have accurate measurements, so the technique has only been employed in very special cases (Czerny et al. 2011; Done et al. 2013). In the case of QPOs, the insufficient observation lengths make the detection of QPOs much more difficult for supermassive black holes than in the case of the stellar-mass ones.

The most prominent feature in the reflection spectrum of the disk is usually the iron Kα line, which is at 6.4 keV in the case of neutral iron atoms and shifts up to 6.97 keV in the case of H-like iron ions. For this reason the technique is also called iron line method, but any measurement should be obtained by fitting the whole reflection spectrum, not only the iron line. The shape of the reflection spectrum encodes information about the ionization and metallicity of the disk, the viewing angle of the disk, and the disk's emissivity (Fabian et al. 1989; Laor 1991; Dovčiak et al. 2004). In the presence of high-quality data and employing the correct astrophysical model, the study of the disk's reflection spectrum can potentially provide accurate measurements of the black hole spin (Brenneman 2013; Reynolds 2014) or even test Einstein's theory of general relativity in the strong gravity regime (Jiang et al. 2015; Bambi 2017).

The reliability of current spin measurements of supermassive black holes using X-ray reflection spectroscopy is a subtle and complicated issue. For instance, the broad-line Seyfert 1 galaxy MCG-06-30-15 has been extensively studied and there are a few different measurements of the spin of its supermassive black hole (Brenneman & Reynolds 2006; Patrick et al. 2012; Walton et al. 2013), ranging from $a_* = 0.5^{+0.2}_{-0.1}$ to $a_* > 0.98$. In the case of the radio galaxy 3C 120, in the same study it is found that a fast-rotating black hole with a co-rotating disk ($a_* = 0.95$) is as likely as a counter-rotating disk ($a_* < 0.10$) (Cowperthwaite & Reynolds 2012; Lohfink et al. 2013). It is also remarkable the vast majority of current estimates of the spins of supermassive black holes find $a_* > 0.8$ (Brenneman 2013; Reynolds 2014).

Most of the spin measurements reported in the literature have been obtained from X-ray data up to 10 keV. However, Bonson & Gallo (2016) have recently shown that the value of the black hole spin can be easily overestimated when the analysis of the reflection spectrum is restricted to the 2-10 keV band, because it is not possible

† Corresponding author: bambi@fudan.edu.cn

to have accurate measurements of the inner emissivity index and of the ionization parameter. When the bandpass is extended up to 70 keV, those parameters can be better constrained, with benefits for the spin measurement too. We can thus expect that more accurate and reliable spin measurements can be obtained, for instance, by employing XMM-Newton and Suzaku data in the 2-10 keV band, because they have a superior sensitivity, in combination with NuSTAR observations, which extend up to 80 keV.

MCG-05-23-16 is a bright nearby ($z = 0.0085$; 36 Mpc) S0/a galaxy, hosting a Seyfert 1.9 nucleus (Ferruit et al. 2000; Raban et al. 2008). It exhibits an X-ray spectrum typical of a Compton-thin Seyfert 2 galaxy, with a soft excess below 1 keV and a moderate photoelectric absorption; the column density is $\sim 1.5 \times 10^{22}$ cm^{-2} (Reeves et al. 2007). This AGN has been extensively analyzed in 0.4-10.0 keV energy band (Weaver et al. 1997; Balestra et al. 2004; Braito et al. 2007; Reeves et al. 2007; Zoghbi et al. 2013) and up to 80 keV (Mattson & Weaver 2004; Reeves et al. 2007; Zoghbi et al. 2014; Baloković et al. 2015; Zoghbi et al. 2017), showing a complex structure of the fluorescent iron line emission, including both broad and narrow components produced, respectively, by the reflection of the accretion disk and the fluorescence and scattering off material in a distant molecular cloud, such as a putative torus; see Reeves et al. (2007) for more details.

There are 15 observations of MCG-05-23-16 with XMM-Newton, Suzaku, and NuSTAR (see Section 2 and Tab. 1). 10 observations have an exposure time longer than 90 ks. The aim of our work is to analyze these 10 observations together in order to obtain the most accurate measurement of the black hole spin parameter a_* by fitting the spectrum in the X-ray broad band 0.5-78 keV. As a consistency check, we have also divided our observations into four epochs, on the basis of their flux hardness ratio, and fitted each epoch spectrum with the same astrophysical model, finding consistent values of the spin parameter.

The content of the paper is as follows. In Section 2, we discuss the observations of MGC-05-23-16 of XMM-Newton, Suzaku, and NuSTAR and how we have reduced the data. In Section 3, we present our results, including light curves, epoch-resolved, and multi-epoch spectral analysis. Section 4 is devoted to the discussion and the conclusions. Throughout the paper, unless stated otherwise, the errors are at the 90% confidence limits for one parameter.

2. OBSERVATIONS AND DATA REDUCTION

Tab. 1 summarizes the observations of MCG-05-23-16 with XMM-Newton, Suzaku, and NuSTAR. Over a period of about 15 years (from May 2001 to December 2015), there are 15 observations. In particular, there are 3 observations of XMM-Newton, 3 observations of Suzaku, and 4 observations of NuSTAR with an exposure time longer than 90 ks. XMM-Newton and Suzaku simultaneously observed the galaxy in December 2005 (ObsID 0302850201 and 700002010), while Suzaku and NuSTAR simultaneously observed the galaxy in June 2013 (ObsID 708021010, 708021020, and 60001046002). In what follows, we only use the data with exposure time longer than 90 ks, in order to have a better statistics. The data have been processed using HEASoft v6.17 and SAS v.14.0.0.

2.1. *XMM-Newton*

There are three XMM-Newton observations of MCG-05-23-16 with a total exposure time over 130 ks (see Tab. 1), using both EPIC CCDs (Strüder et al. 2001; Turner et al. 2001) and the RGS cameras (den Herder et al. 2001). The MOS1 and MOS2 operated in Small-Window mode; the pn was in Small-Window (ObsId 0727960101 and 0727960201) and Large-Window (ObsId 0302850201) modes. We followed the standard data reduction procedures to process and clean XMM-Newton data using SAS. In order to define a threshold to filter out the high-background time intervals, we extracted the single events 10-12 keV light curves and filtered out the data when the light curve is 3σ above its mean. The net exposure times are shown in Tab. 1. Taking into account the brightness of source, we ran the SAS task epatplot to check for possible pileup, and we found that in MOS detectors the pileup fraction is 3%-8%, and in pn detectors the pileup fraction is below 1%. We decided therefore to use only the EPIC-pn spectra for the analysis discussed in this paper.

The EPIC-pn source spectra were extracted using a circular region of $40''$ centered at the galaxy center (J2000, 09h 47m 40.1s, -30m 56h 55s), and background spectra were extracted using a circle with the same radius centered at $\sim 2'$ from the source. As standard procedure in X-ray spectroscopy at moderate spectral resolution, we binned the spectra to have at least 30 background-subtracted counts in each spectral channel. The signal-to-noise ratio per bin in the 1.0-8.0 keV range is above 50 to ensure that we can use the χ^2 goodness-of-fit test. Response matrices and ancillary response files at the source position were created using the SAS tasks arfgen and rmfgen.

We fit the EPIC-pn spectra in the 0.5-7.5 keV band, to avoid a systematic count excess (at the 5% level) above 7.5 keV when the best-fit baseline model is applied to the multi-epoch fits. The origin of this excess is unknown. Systematic excesses at this level were observed in papers studying the effective area cross-calibration among flying instruments in that energy range (Ishida et al. 2011; Madsen et al. 2017), even if such results are probably dominated by uncertainties in the calibration of the wings of the Point Spread Function (Read et al. 2011). In our multi-epoch fits, we take advantage of the higher effective area of NuSTAR in the 7.5-10 keV energy range to constrain the best-fit model.

2.2. *Suzaku*

Suzaku observed MCG-05-23-16 with its X-ray Imaging Spectrometer (XIS) and Hard X-ray Detector (HXD) PIN instruments in December 2005 and June 2013. Our reduction follows the recommendations of the Suzaku Data Reduction Guide (http://heasarc.gsfc.nasa.gov/docs/suzaku/analysis/).

For XIS, we generated cleaned event files for each operational detector (XIS0, XIS1, XIS2, and XIS3) in both editing modes (3×3 and 5×5) using the Suzaku AEPIPELINE with the latest calibration, as well as the associated screening criteria files in HEASoft. We did not reprocess the Suzaku Hard X-ray Detector (HXD) PIN

instrument data because of its lower sensitivity than that of NuSTAR.

As Suzaku observed MCG-05-23-16 in a relatively bright state, we assessed the influence of pileup in the XIS data using the pileest script. We found that, for XIS0, XIS1, and XIS3 the central $\sim 30''$ has a pileup fraction 3%-10% assuming a grade migration parameter of 0.5. Thus, we excluded the central $\sim 30''$ regions to minimize the pileup influence in the light curve and spectral analyses.

Using the addascaspec we co-added spectra extracted from the XIS front-illuminated (XIS-FI) detectors, XIS0 and XIS3, in an annular region of $30''$-$80''$. Background spectra were extracted using an annulus with the same inner and outer radius in a nearby region. We binned XIS source spectra into channels with a minimum of 30 counts per bin using grappha. XIS1 and XIS2 were not used owing to the higher background level at high energies.

Spectral fits used the added data from XIS0 and XIS3 in the energy range 0.8-10.0 keV. Data in the range 1.7-2.0 keV were excluded from the XIS spectral analysis because of the uncertainties in calibration around the instrumental Si K edge. In order to employ the χ^2 statistics, we regroup the data to have a signal-to-noise ratio of 50 per bin after background subtraction.

2.3. *NuSTAR*

We reprocessed the NuSTAR Level 1 data using the standard pipeline [NUPIPELINE; Perri et al. (2015)] from the NuSTAR data analysis software (NuSTARDAS v1.5.1) within the HEASoft package (v6.17) and CALDB (20150306). We then used the NUPRODUCTS program to extract light curves and spectra from the cleaned event lists for both focal plane modules FPMA and FPMB. We filtered out the data when the light curve is 5σ above its mean. The source spectra were extracted from circular regions $120''$ in radius, centered at the peak of the source image. The corresponding background spectra were extracted from a near circular region with the same radius.

We fitted the NuSTAR data over the whole energy range of 3.0-78.0 keV. The spectra were binned to have at least 30 counts in each energy bin. In order to employ the χ^2 statistics, we regroup the data to have a signal-to-noise ratio of 50 per bin after background subtraction.

3. RESULTS

3.1. *Light Curves and Hardness Ratio*

Fig. 1*a* shows the light curves of MCG-05-23-16 in the 2.0-10.0 keV band of the 10 observations with exposure time longer than 90 ks (see Tab. 1) binned to 5760 s. The light curves are background-subtracted and have been corrected by the response effective area based on the spectrum best-fit. For the Suzaku data, we have converted the count rate to the flux by multiplying it by 4.95×10^{11} ergs cm^{-2} count^{-1}. In order to directly compare count rates measured by different instruments, we have normalized the count rates of XMM-Newton to the Suzaku flux multiplying them by the count-to-flux factor mentioned above, augmented by a further factor 2.52, which is computed from the ratio between the spectral fluxes of XMM-Newton and Suzaku. Employing the same method, we have also converted the NuSTAR broadband count rates into fluxes by multiplying the count rates-derived fluxes by a further factor 1.14 and 1.04, respectively for FPMA and FPMB.

In Fig. 1, the 2.0-10.0 keV flux from December 2005 to Match 2015 shows a variability by a factor of four: from 7.7×10^{-11} ergs cm^{-2} s^{-1} to 28.3×10^{-11} ergs cm^{-2} s^{-1}. Such a variability is similar to that seen in previous observations, from $\sim 20 \times 10^{-11}$ ergs cm^{-2} s^{-1} in 1978 (Tennant 1983) to $\sim 5 \times 10^{-11}$ ergs cm^{-2} s^{-1} in 1989 (Nandra & Pounds 1994), and again to $\sim 23 \times 10^{-11}$ ergs cm^{-2} s^{-1} in 1994-2000 (Weaver et al. 1998; Balestra et al. 2004) .

In order to obtain the variability of the hardness ratio, we plot the flux light curves in the 2.0-4.0 keV (Fig. 1*a*) and 4.0-10.0 keV (Fig. 1*b*) bands. The flux in the 2.0-4.0 keV energy range exhibits a dynamical range of about a factor of five, while the flux in 4.0-10.0 keV energy range exhibits a dynamical range of a factor of three only. This demonstrates that the flux variability of the galaxy occurs mainly in the soft X-ray band. The hardness ratio varies from 1.1 to 2.2, with the value 1.3-1.4 in December 2005, 1.1-2.2 in June 2013, and 1.7-2.0 in February-March 2015. The hardness ratio in June 2013 clearly presents two different values, 1.1-1.3 in the XMM-Newton data and 1.8-2.2 in the Suzaku and NuSTAR data.

According to the hardness ratio light curves, we divide our data into four epochs named E1 (December 2005), E2 (June 2013, Suzaku and NuSTAR observations), E3 (June 2013, XMM-Newton observations), and E4 (February-March 2015).

3.2. *Spectral Modelling*

The broad-band XMM-Newton pn, Suzaku XIS, and NuSTAR FPMA and FPMB spectra in the 0.5-78.0 keV energy range are shown in Fig. 2. The difference between these spectra is greatest at about 2 keV.

MCG-05-23-16 has a complex structure of the fluorescent iron Kα line, including both a broad and a narrow components produced, respectively [see Reeves et al. (2007)], by the disk's reflection and by a distant molecular torus. We have therefore builded a double-reflection spectral model as TBabs×[zWabs1×(Cutoffpl+Relxill)+zWabs2×Xillver +Apec+Apec], where TBabs is fixed at the averaged Galactic absorption of the galaxy [8.7×10^{20} cm^{-2}; Kalberla et al. (2005)]. Here Relxill (Dauser et al. 2010, 2014; García et al. 2014) is used to describe the disk's reflection spectrum, while Xillver (García & Kallman 2010; García et al. 2013) describes the reflected component from the molecular torus. We allow the column densities covering these components to be different. We use two collisionally ionised, equilibrium components [Apec; Foster et al. (2012)] to describe the soft X-ray excess. A power-law component (Cutoffpl) describes the corona emission. When we fit the spectra, we bind the power-law parameters of Relxill and Xillver to those of Cutoffpl. In our fits, the photon index and the high energy cut-off of the power-law are free, as well as the parameters of emissivity profile (Index1, Index2, and Rbr in Relxill), the ionization parameter[1], the

[1] $\xi = \frac{L}{nr^2}$, where L is the ionizing luminosity, n the electron density, and r^2 the distance between the disk surface and the source

inclination angle of the disk, the black hole spin, and the temperatures of the thermal components. The inner edge of the accretion disk is assumed to be at the innermost stable circular orbit, while the outer edge is set at 400 gravitational radii. The metal abundance is a single free parameter in the fit. The redshift of the galaxy MCG-05-23-16 is fixed at $z = 0.0085$, while the redshift in XILLVER is free because we do not know the actual nature of this reflected component. Instead of the reflection spectrum from a torus around the black hole, it may originate in a bi-conical outflow (Elvis 2000) or from the outer disk in a scenario with a warped disk (Nayakshin 2005).

3.2.1. *Epoch-resolved spectral analysis*

In order to study possible evolutions of the accretion disk and the consistency of our model, here we separately analyze the four epoch spectra of MCG-05-23-16. The best-fitting spectra are shown in Fig. 3, and the corresponding models are presented in Tab. 2. Since the ionization parameter $\log \xi$ cannot be constrained from the multi-epoch spectrum (see Subsection 3.2.2), here we fix $\log \xi$ to 0. We set the metal abundance to the best-fit value of the multi-epoch spectrum (see Subsection 3.2.2). Since the high energy cut-off cannot be constrained by fitting the spectra below 10 keV, we fix it to the best-fit value of the multi-epoch spectrum (see Subsection 3.2.2) in E1 and E3. We leave it as a free parameter in E2 and E4, where NuSTAR spectra are available.

For E2 and E4, we only use one Apec component to describe the soft X-ray excess, because the lower temperature component is not required by the fit. For E3, we exclude the energy band 2.2-2.3 keV from the fitting of the EPIC-pn spectrum due to calibration uncertainties at the Au-M photo-absorption edges of the XMM-Newton telescopes (Smith et al. 2013), and the 7.5-10.0 keV energy band where the spectra present high residuals as discussed in the Subsection 2.1 (including this energy range in the E3 fit does not change any of the main conclusions of this paper). In this way we reduce the χ^2 to an acceptable level (χ^2/d.o.f. < 2.0).

All the fits are good with χ^2/d.o.f. < 1.7 (see Tab. 2) and show low residuals in the 4.0-10.0 keV range (see Fig. 3). The estimates of the black hole spin and disk inclination angle are: $a_* < 0.90$ and $i = 59.1^{+3.9}_{-5.0}$ for E1, $a_* = 0.86 \pm 0.02$ and $i = 60.6^{+0.9}_{-0.7}$ for E2, $a_* = 0.82^{+0.02}_{-0.01}$ and $i = 60.8 \pm 0.7$, and $a_* = 0.89^{+0.01}_{-0.05}$ and $i = 62.9^{+1.0}_{-1.5}$ for E4. See Fig. 4. The results indicate that no appreciable difference is found in the estimates both of the black hole spin and disk inclination angle, lending credibility to our spectral parametrization.

As shown in Table 2, the best-fit models for E3 give high values for the emissivity indices (Index1 & Index2) together with a smaller breaking radius (Rbr). When we fix the three emissivity parameters and disk inclination angle to the best-fit values of multi-epoch spectra (see Subsection 3.2.2), the χ^2/d.o.f. is 459.1/252. Using the F-test, this solution can be excluded at 99.9% confidence, which means the emissivity of the accretion disk in E3 is significantly different from that of the time-averaged multi-epoch spectra.

of ionizing continuum.

As we can see in Table 2, the best-fit value of the redshift in XILLVER for E3 is significantly lower than that of the galaxy MCG-05-23-16 ($z = 0.0085$). If we fix the redshift in XILLVER at 0.0085, the χ^2/d.o.f. is 542.1/249. Using the F-test, this solution can be excluded at 99.9% confidence, which suggests that the astrophysical system modeled by the XILLVER component may be moving towards us in E3.

Since E2 and E4 have a similar value of the hardness ratio (see Fig. 1) and Zoghbi et al. (2017) also suggested no significant difference among the spectra in E2 and E4, we compare the best-fit spectrum models in E2 and E4 shown in Table 2. With the exception of the photon index (Γ), the absorption (zWabs1) in RELXILL, the absorption (zWabs2), and the redshift in XILLVER show possible differences. We fit the spectra in E2 and E4 together with the photon index (Γ), the absorption (zWabs1) in RELXILL, as well as the absorption (zWabs2) and the redshift in Xillver as free parameters for each epoch. The best-fit model is shown in Table 2 and the χ^2/d.o.f. is 12317.3/11529. No difference of the best-fit zWabs1 is found. We then fit the E2 and E4 spectra with Γ, Γ and zWabs2, and Γ and the redshift in XILLVER as free parameters for each epoch, respectively, and the corresponding χ^2/d.o.f. are 12414.3/11533, 12379.8/11532, and 12384.9/11532. Using F-test, we find that the absorption (zWabs2) and the redshift in XILLVER between E2 and E4 are significantly different at 99.9% confidence.

3.2.2. *Multi-epoch spectral analysis*

In order to obtain the most accurate measurements of the parameters of the system, we fit all the spectra simultaneously with the above double-reflection model. The spectra and best-fit models are shown in Fig. 5 and in Table 2. As the photon index (Γ), the absorption (zWabs2) and redshift in XILLVER clearly show to be different at different epochs, we set these three parameters for each epoch as free.

At first, we fix the high energy cut-off to 300 keV and the metal abundance to 1.0. As shown in Tab. 2, the best-fit χ^2/d.o.f. is 1.22 (15862.3/13018). Because the ionization parameter $\log \xi$ (< 0.4) is not well constrained, we then fix it to 0. When we allow the high energy cut-off and metal abundance to be free, the fit is significantly improved and the χ^2/d.o.f. is 15558.8/13017. Here the best fit value of the high energy cut-off is 168 ± 9 keV and that of the metal abundance is $0.90^{+0.02}_{-0.03}$ $Z_\odot$. The spin parameter of the supermassive black hole $a_* = 0.856 \pm 0.003$ and the inclination angle of the disk $i = 61.4^{+0.3}_{-0.2}$. The best-fit absorption (zWabs1) is $1.53 \pm 0.01 \times 10^{22}$ cm^{-2}, which is consistent with those in Weaver et al. (1997); Balestra et al. (2004); Reeves et al. (2007). The best-fit metal abundance is $0.90^{+0.02}_{-0.03}$ $Z_\odot$, which is consistent with the previous results (Zoghbi et al. 2017). Due to the known correlations between the black hole spin and the abundance (Reynolds et al. 2012), we calculated the iso-χ^2 contours between these two quantities (Fig. 6). The spin parameter of the supermassive black hole is $a_* = 0.856 \pm 0.006$ at 99% confidence for two interesting parameters.

4. DISCUSSION AND CONCLUSIONS

In our multi-epoch and multi-instrument study of the supermassive black hole at the center of the galaxy MCG-05-23-16, we have analyzed high quality data of XMM-Newton, Suzaku, and NuSTAR in order to obtain an accurate measurement of the black hole spin parameter. We have restricted our attention to the 10 observations with exposure time longer than 90 ks. MCG-05-23-16 has a moderate absorbed spectrum with a complex structure of the fluorescent iron line emission, including both a broad and a narrow component. Consequently, we have constructed a standard AGN astrophysical model with two reflection components: one broadened by relativistic effects, describing emission from the innermost regions of the accretion disk, and another describing the reflection off distant matter (the "torus"). This model fits satisfactorily the multi-epoch spectra.

Our measurement of the black hole spin parameter is $a_* = 0.856 \pm 0.006$ (99% confidence level for two interesting parameters). We have also split the data in four epochs and found that the analyses of the spectra of each epoch provide consistent results, with the same spin measurement at the 90% confidence level. This lends confidence to the reliability of our spectral parameterization (Walton et al. 2013).

There are no previous measurements in the literature of the spin parameter of the black hole in MCG-5-23-16, so it is not possible to compare our result with that of other authors. However, it can be useful to briefly remind the possible systematic errors in this kind of measurements. The key assumption in the reflection model is that the accretion disk around the black hole is geometrically thin and that the inner edge of the disk is at the innermost stable circular orbit. In the case of black hole binaries, these conditions should be satisfied when the source is in the soft state and the accretion luminosity is roughly between 5% and 20-30% of the Eddington limit (McClintock et al. 2006, 2014)[2]. The assumption concering the innermost stable circular orbit is well supported by numerical simulations (Kulkarni et al. 2011) and by the observed constancy of the inner edge of the disk over many years for the same sources (Steiner et al. 2010). When the source is in the hard state, the situation is more tricky, but it is still possible to identify observations in which the inner edge of the disk should be at the innermost stable circular orbit by comparing observations of the same source at different times (García et al. 2015).

In the case of AGN, it is definitively more difficult to check if these conditions are satisfied. The uncertainties on the measurements of the mass and the distance of the black hole are large and systematics effects are possible. Even the estimate of the total accretion luminosity is problematic. In the end, it is not possible to conclude if the source is at the right accretion rate to expect that the disk is thin and that its inner edge is at the innermost stable circular orbit. For lower accretion luminosities, the disk may be truncated at a larger radius, which would lead to underestimate the black hole spin. For higher accretion luminosities, the inner part of the disk is not geometrically thin, the inner edge may be at a radius smaller than the innermost stable circular orbit, and the measurement would overestimate the black hole spin. In the case of AGN, because of the different timescales with respect to black hole binaries, it is also impossible to check the stability of the inner edge of the disk. In practice, if there is a broad iron line, we apply the model valid for thin disks without the possibility of checking if this is correct.

It is also difficult to estimate the uncertainty of the spin measurement due to systematic effects, so it is common to only express the statistical error. Using high-resolution 3D MHD simulations of a geometrically thin accretion disk, Reynolds & Fabian (2008) constructed a model to estimate the systematic errors on black hole spin measurements from the emission inside the inner edge of the disk. They found that the systematic errors can be significant for slow-rotating black holes but decrease as the spin parameter increases. The actual thickness of the disk also plays an important rule for the spin estimate of slow-rotating black holes, while the impact of the viewing angle on the systematic errors is very small.

Bearing in mind that our measurement may be affected by these systematic effects, we can try to discuss its implications. First, our measurement is consistent with the idea that most AGN host rapidly spinning supermassive black holes with $a_* > 0.8$ (Reynolds 2014). This may further support the belief that at least the recent stage of the accretion of these objects has occurred via prolonged disk accretion and not from chaotic accretion or mergers (Berti & Volonteri 2008). Second, there is currently some weak evidence that supermassive black holes in AGN with a mass in the range $2 \times 10^6\ M_\odot$ and a few $10^7\ M_\odot$ have a spin parameter very close to 1, say $a_* > 0.9$, while that of lighter and heavier objects is lower, say $a_* \sim 0.6$-0.9, see Fig. 6 in Reynolds (2014). The mass of the black hole in MCG-5-23-16 has been estimated to be $M \sim 2 - 8 \times 10^7\ M_\odot$ (Ponti et al. 2012). Our measurement of the black hole spin of MCG-5-23-16 seems to fit this thesis. If this were indeed the case, we may argue that chaotic accretion or mergers may play a more important role for lighter and heavier black holes.

This work was supported by the National Natural Science Foundation of China (Grants No. 11103057, U1531117, and 11305038) and the Thousand Young Talents Program. M.G.-N. also acknowledges the support from the China Scholarship Council (Grant No. 2014GXZY08). C.B. also acknowledges the support from the Alexander von Humboldt Foundation.

[2] Ricci et al. (2013) have estimated the luminosity of MCG-5-23-16 to be 3.2% of its Eddington limit.

REFERENCES

Balestra, I., Bianchi, S., & Matt, G. 2004, A&A, 415, 437
Baloković, M., Matt, G., Harrison, F. A., et al. 2015, ApJ, 800, 62
Bambi, C. 2017, Reviews of Modern Physics (in press) [arXiv:1509.03884]
Berti, E., & Volonteri, M. 2008, ApJ, 684, 822-828
Bonson, K., & Gallo, L. C. 2016, MNRAS, 458, 1927
Braito, V., Reeves, J. N., Dewangan, G. C., et al. 2007, ApJ, 670, 978
Brenneman, L. W., & Reynolds, C. S. 2006, ApJ, 652, 1028
Brenneman, L. 2013, *Measuring the Angular Momentum of Supermassive Black Holes*, SpringerBriefs in Astronomy. ISBN 978-1-4614-7770-9
Cowperthwaite, P. S. & Reynolds, C. S. 2012, ApJ, 752, L21
Czerny, B., Hryniewicz, K., Nikołajuk, M., & Sądowski, A. 2011, MNRAS, 415, 2942
Dauser, T., Wilms, J., Reynolds, C. S., and Brenneman, L. W. 2010, MNRAS 409, 1534
Dauser, T., García, J., Parker, M. L., Fabian, A. C. & Wilms, J. 2014, MNRAS, 444, L100
den Herder, J. W., Brinkman, A. C., Kahn, S. M., et al. 2001, A&A, 365, L7
Done, C., Jin, C., Middleton, M., & Ward, M. 2013, MNRAS, 434, 1955
Dovčiak, M., Karas, V., & Yaqoob, T. 2004, ApJS, 153, 205
Elvis, M. 2000, ApJ, 545, 63
Fabian, A. C., Rees, M. J., Stella, L., & White, N. E. 1989, MNRAS, 238, 729
Ferruit, P., Wilson, A. S., & Mulchaey, J. 2000, ApJS, 128, 139
Foster, A. R., Ji, L., Smith, R. K. & Brickhouse, N. S 2012, ApJ, 756, 128
García, J. & Kallman, T. R. 2010, ApJ, 718, 695
García, J., Dauser, T., Reynolds, C. S., Kallman, T. R., McClintock, J. E., Wilms, J. & Eikmann, W. 2013, ApJ, 768, 146
García, J., Dauser, T., Lohfink, A., Kallman, T. R., Steiner, J. F., McClintock, J. E., Brenneman, L., Wilms, J., Eikmann, W., Reynolds, C. S., and Tombesi, F. 2014, ApJ 782, 76
García, J. A., Steiner, J. F., McClintock, J. E., et al. 2015, ApJ, 813, 84
Ishida, M., Tsujimoto, M., Kohmura, T., Stuhlinger, M., Smith, M., Marshall, H. L., Guainazzi, M., Kawai, K., and Ogawa, T. 2011, PASJ, 63, S657
Jiang, J., Bambi, C., & Steiner, J. F. 2015, ApJ, 811, 130
Kalberla, P. M. W., Burton, W. B., Hartmann, D., et al. 2005, A&A, 440, 775
Kulkarni, A. K., Penna, R. F., Shcherbakov, R. V., et al. 2011, MNRAS, 414, 1183
Laor, A. 1991, ApJ, 376, 90
Lohfink, A. M., Reynolds, C. S., Jorstad, S. G., et al. 2013, ApJ, 772, 83
Madsen, K. K., Beardmore, A. P., Forster, K., et al. 2017, AJ, 153, 2
Mattson, B. J., & Weaver, K. A. 2004, ApJ, 601, 771
McClintock, J. E., Narayan, R., Davis, S. W., et al. 2011, Classical and Quantum Gravity, 28, 114009
McClintock, J. E., Narayan, R., & Steiner, J. F. 2014, Space Sci. Rev., 183, 295
McClintock, J. E., Shafee, R., Narayan, R., et al. 2006, ApJ, 652, 518
Motta, S. E., Belloni, T. M., Stella, L., Muñoz-Darias, T., & Fender, R. 2014, MNRAS, 437, 2554
Nandra, K., & Pounds, K. A., 1994, MNRAS, 268, 405
Narayan, R. 2005, New Journal of Physics, 7, 199
Nayakshin, S. 2005, MNRAS, 359, 545
Patrick, A. R., Reeves, J. N., Porquet, D., et al. 2012, MNRAS, 426, 2522
Perri, M., Puccetti, S., Spagnuolo, N, et al. 2015, The NuSTAR Data Analysis Software Guide, http://heasarc.gsfc.nasa.gov/docs/nustar/analysis/nustar_swguide.pdf
Ponti, G., Papadakis, I., Bianchi, S., et al. 2012, A&A, 542, A83
Raban, D., Heijligers, B., Röttgering, H., et al. 2008, A&A, 484, 341
Read, A. M., Rosen, S. R., Saxton, R. D., & Ramirez, J. 2011, A&A, 534, A34
Reeves, J. N., Awaki, H., Dewangan, G. C., et al. 2007, PASJ, 59, S301
Reynolds, C. S. 2014, Space Sci. Rev., 183, 277
Reynolds, C. S., Brenneman, L. W., Lohfink, A. M., et al. 2012, ApJ, 755, 88
Reynolds, C. S., & Fabian, A. C. 2008, ApJ, 675, 1048-1056
Ricci, C., Paltani, S., Ueda, Y., & Awaki, H. 2013, MNRAS, 435, 1840
Smith, M., Guainazzi, M., & Marinucci, A. 2013, XMMCCF-REL-300
Steiner, J. F., McClintock, J. E., Remillard, R. A., et al. 2010, ApJ, 718, L117
Strüder, L., Briel, U., Dennerl, K., et al. 2001, A&A, 365, L18
Tennant, Jr. A. F., 1983 Ph.D. Thesis
Török, G., Abramowicz, M. A., Kluźniak, W., & Stuchlík, Z. 2005, A&A, 436, 1
Turner, M. J. L., Abbey, A., Arnaud, M., et al. 2001, A&A, 365, L27
Wagoner, R. V., Silbergleit, A. S., & Ortega-Rodríguez, M. 2001, ApJ, 559, L25
Walton, D. J., Nardini, E., Fabian, A. C., Gallo, L. C., & Reis, R. C. 2013, MNRAS, 428, 2901
Weaver, K. A., Krolik, J. H., & Pier, E. A. 1998, ApJ, 498, 213
Weaver, K. A., Yaqoob, T., Mushotzky, R. F., et al. 1997, ApJ, 474, 675
Zhang, S. N., Cui, W., & Chen, W. 1997, ApJ, 482, L155
Zoghbi, A., Reynolds, C., Cackett, et al. 2013, ApJ, 767, 121
Zoghbi, A., Cackett, E. M., Reynolds, C., et al. 2014, ApJ, 789, 56
Zoghbi, A., Matt, G., Miller, J. M., et al. 2017, accepted for publication in ApJ

TABLE 1
X-ray Observations of MCG-05-23-16

X-ray Mission	Obs_ID	Obs_time	Exposure Time (ks)	Net Exposure Time[a] (ks)
XMM-Newton	0112830301	2001-05-13	38.4	–
	0112830401	2001-12-01	24.9	–
	0112830701	2001-12-01	9.3	–
	0312850201	2005-12-08	131.7	95.4
	0312850301	2005-12-10	4.4	–
	0727960101	2013-06-24	138.4	96.2
	0727960201	2013-06-26	139.0	110.4
Suzaku	700002010	2005-12-07	95.7	95.7
	708021010	2013-06-01	159.5	159.5
	708021020	2013-06-05	138.8	138.8
NuSTAR	10002019001	2012-07-11	33.9	–
	60001046002	2013-06-03	160.5	160.0/160.5
	60001046004	2015-02-15	210.9	210.9/210.6
	60001046006	2013-02-21	98.4	98.4/98.1
	60001046008	2013-03-13	220.8	219.5/219.3

[a] Net exposure time for XMM-Newton pn, Suzaku XIS, and NuSTAR FPMA/FPMB after data screening. Only observations corresponding to table rows with an entry in the rightmost column have been analyzed in this paper.

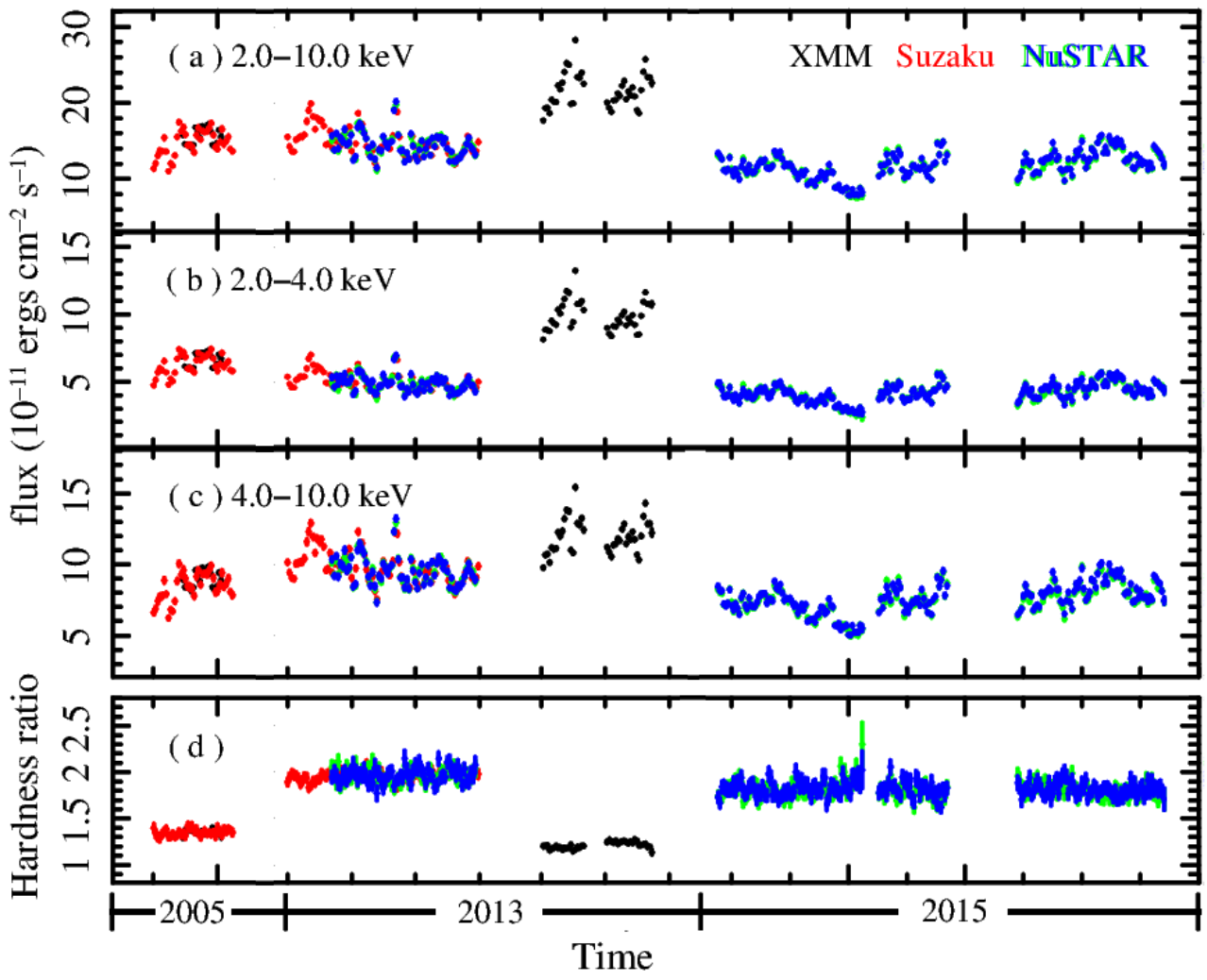

FIG. 1.— Light curves of MCG-05-23-16 in 2.0-10.0 keV band (panel *a*), 2.0-4.0 keV band (panel *b*), and 4.0-10.0 keV band (panel *c*) of the 10 observations with exposure time longer than 90 ks (see Tab. 1) binned to 5760 s. All of the data have subtracted background and have been corrected by the response effective area based on the spectrum best-fittings (details in the text). The hardness ratio distribution (panel *d*) is calculated from the 4.0-10.0 keV and 2.0-4.0 keV fluxes.

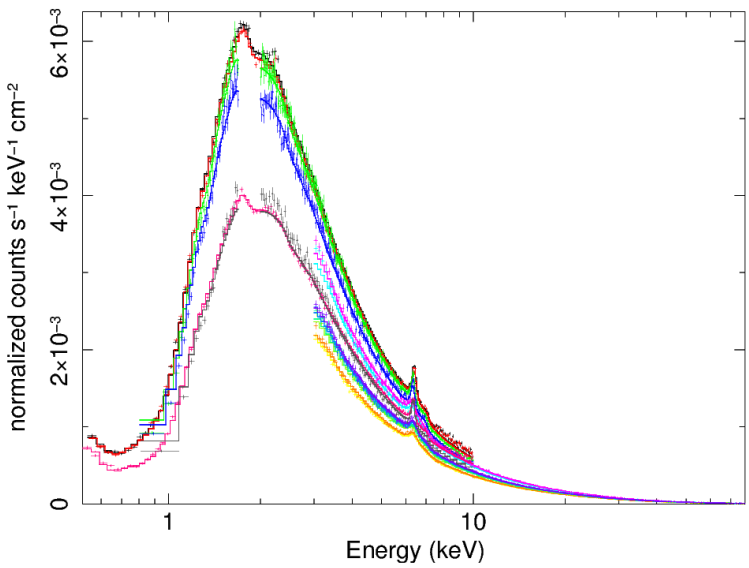

FIG. 2.— The broad-band XMM-Newton pn, Suzaku XIS, and NuSTAR FPMA and FPMB spectra in 0.5-78.0 keV band. Spectra were corrected by the effective areas. The difference between these spectra is greatest at about 2 keV. The spectra of Suzaku and NuSTAR are rebinned to oversample the spectral resolution by a factor 20 or to a minimum signal to noise of 50 after background subtraction.

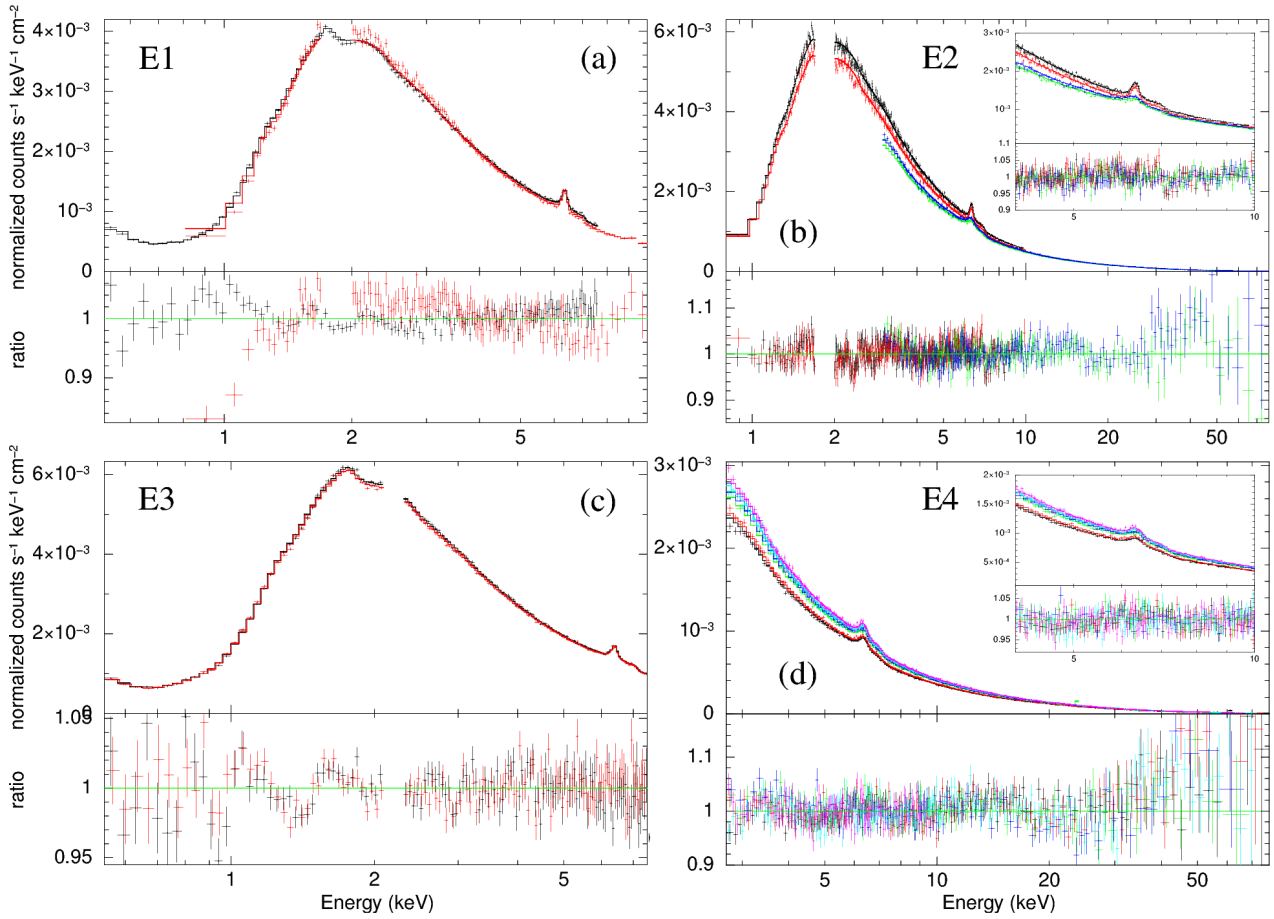

FIG. 3.— The X-ray spectra (upper panels), and residuals against the best-fit model in data/model ratio (lower panels) of MCG-05-23-16 in E1 (*a*), E2 (*b*), E3 (*c*), and E4 (*d*), respectively. In E1, XMM-Newton data is shown as black and the red is Suzaku data; In E2, XMM-Newton data are shown as black and red, NuSTAR data are shown as green and blue; In E3, all are XMM-Newton data; and in E4, all are NuSTAR data. For clarity, we also shown the spectra and their best-fits in 4.0-10.0 keV for E2 and E4.

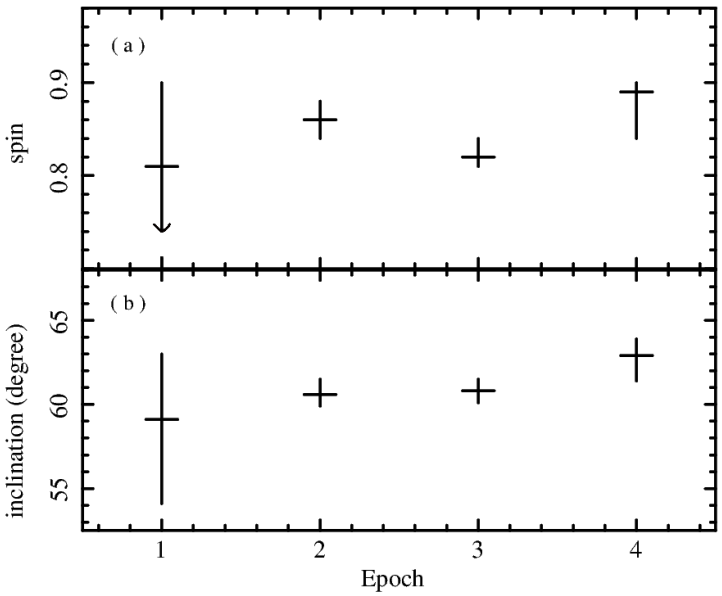

FIG. 4.— The best-fit values of the black hole spin (a) and disk inclination angle (b) for each epoch.

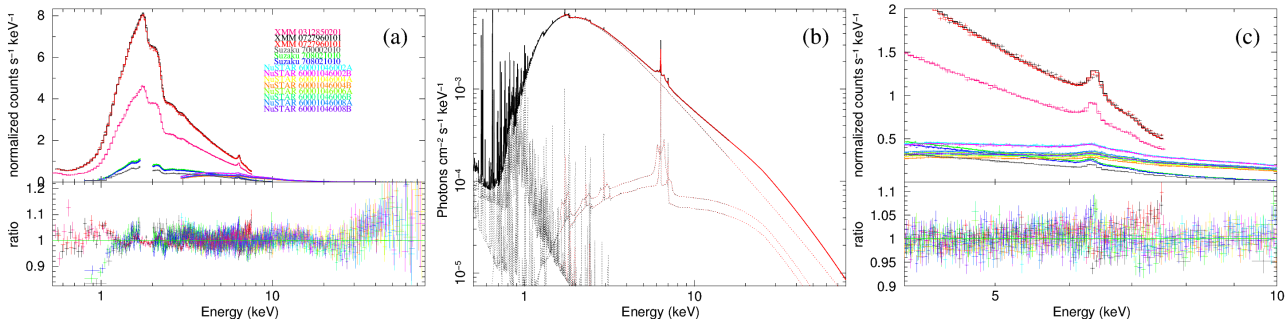

FIG. 5.— Panel (a): The total X-ray spectrum of MCG-05-23-16 in the 0.5-78.0 keV energy range for the 10 observations with exposure time longer than 90 ks (see Tab. 1) and its best-fit. Panel (b): The best fit model of the multi-epoch spectrum shown in panel (a). Panel (c): The multi-epoch spectrum in the 4.0-10.0 keV energy range.

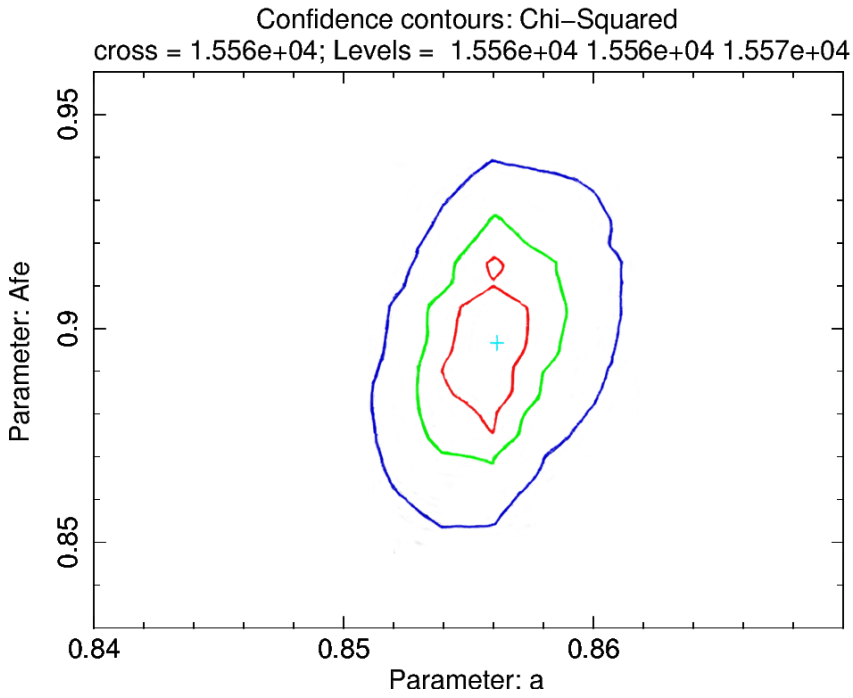

FIG. 6.— The iso-χ^2 contours between Fe abundance and black hole spin for the multi-epoch spectral analysis. The cyan cross shows the location of the best-fit values. The red, green, and blue lines are corresponding, respectively, to the 68%, 90%, and 99% confidence levels.

TABLE 2
BEST-FITS FOR THE EPOCH-RESOLVED AND MULTI-EPOCH SPECTRAL ANALYSIS

Epoch	Γ[1]	HighECut keV	Index1	Index2	Rbr R_g	spin	Incl degree	T1 keV	T2 keV	zWabs1 10^{22}cm^{-2}	zWabs2[2] 10^{22}cm^{-2}	Δz[3] 10^{-3}	χ^2/d.o.f
E1	1.86 ± 0.02	(168)	< 60	1.6 ± 0.3	< 3.0	$0.81^{+0.09}_{-0.81}$	$59.1^{+3.9}_{-5.0}$	0.26 ± 0.03	0.99 ± 0.05	1.56 ± 0.02	< 0.12	$-1.3^{+0.7}_{-0.9}$	1862.6/1396
E2	1.97 ± 0.01	160^{+16}_{-15}	34 ± 4	$0.7^{+0.2}_{-0.3}$	$3.5^{+0.1}_{-0.2}$	0.86 ± 0.02	$60.6^{+0.9}_{-0.7}$	$0.78^{+0.08}_{-0.07}$	–	$1.56^{+0.02}_{-0.01}$	$8.4^{+2.1}_{-2.2}$	1.1 ± 0.9	6049.1/5570
E3	$1.97^{+0.02}_{-0.01}$	(168)	60^{+8}_{-9}	$1.8^{+0.2}_{-0.1}$	3.1 ± 0.1	$0.82^{+0.02}_{-0.01}$	60.8 ± 0.7	0.23 ± 0.03	0.99 ± 0.03	1.50 ± 0.02	0.20 ± 0.03	< -6.3	411.7/248
E4	1.91 ± 0.02	175^{+10}_{-9}	41^{+11}_{-14}	< 0.5	3.5 ± 0.2	$0.89^{+0.01}_{-0.05}$	$62.9^{+1.0}_{-1.5}$	0.55 ± 0.05	–	$3.0^{+0.3}_{-0.2}$	<2.5	$-5.8^{+2.3}_{-1.2}$	6118.8/5795
E2+E4	1.98 ± 0.01 (E2)	159^{+11}_{-10}	28^{+5}_{-3}	0.5 ± 0.2	$3.5^{+0.2}_{-0.3}$	$0.88^{+0.02}_{-0.01}$	$62.5^{+0.9}_{-0.7}$	0.80 ± 0.08	–	1.57 ± 0.01 (E2)	$10.7^{+1.9}_{-2.2}$ (E2)	$1.1^{+0.9}_{-0.8}$ (E2)	12317.3/11529
	1.83 ± 0.01 (E4)									1.25 ± 0.09 (E4)	<0.6 (E4)	$-5.2^{+1.7}_{-1.1}$ (E4)	
Multi1[4]	1.86 ± 0.01 (E1)	(300)	45 ± 2	$0.35^{+0.05}_{-0.15}$	$3.39^{+0.05}_{-0.04}$	$0.870^{+0.005}_{-0.006}$	$61.4^{+0.3}_{-0.2}$	$0.23^{+0.03}_{-0.02}$	0.97 ± 0.03	1.55 ± 0.01	0.15 ± 0.02 (E1)	-1.3 ± 0.8 (E1)	15862.3/13018
	1.95 ± 0.01 (E2)										$1.1^{+0.3}_{-0.4}$ (E2)	$1.9^{+0.9}_{-1.0}$ (E2)	
	1.97 ± 0.01 (E3)										$0.24^{+0.02}_{-0.03}$ (E3)	< -7.3 (E3)	
	1.88 ± 0.01 (E4)										<0.4 (E4)	$-2.9^{+2.4}_{-1.7}$ (E4)	
Multi2[5]	1.84 ± 0.01 (E1)	168 ± 9	45 ± 2	$0.36^{+0.05}_{-0.06}$	3.40 ± 0.02	0.856 ± 0.003	$61.4^{+0.3}_{-0.2}$	0.23 ± 0.02	$0.96^{+0.02}_{-0.03}$	1.53 ± 0.01	$0.17^{+0.01}_{-0.02}$ (E1)	$-1.3^{+0.7}_{-0.9}$ (E1)	15558.8/13017
	1.96 ± 0.01 (E2)										1.2 ± 0.4 (E2)	$1.6^{+1.0}_{-1.1}$ (E2)	
	1.98 ± 0.01 (E3)										$0.25^{+0.03}_{-0.02}$ (E3)	< -7.4 (E4)	
	1.88 ± 0.01 (E4)										<0.4 (E4)	$-4.3^{+2.3}_{-1.4}$ (E4)	

[a]Power law index of the Cutoffpl component for E1, E2, E3, and E4, respectively.
[b]Absorption corresponding to the XILLVER component for E1, E2, E3, and E4, respectively.
[c]The Redshift differences against the systemic redshift of galaxy MCG-05-23-16 ($z = 0.0085$) of the XILLVER component for E1, E2, E3, and E4, respectively.
[d]The metal abundance is fixed to 1.0. The best-fit value of the ionization parameter of the RELXILL component is < 0.4. Because the ionization parameter is not well constrained in Multi1, in the other fits it was fixed to 0.
[e]The best-fit value of the metal abundance is $0.90^{+0.02}_{-0.03}$ $Z_\odot$, and we fixed the metal abundance to its best-fit value for every epoch analysis.